RATCHETING OF INTERNALLY PRESSURIZED CORRODED PIPES UNDER CYCLIC BENDING

Marcos André Baêta Neves Silveira, e-mail: mbaeta@lts.coppe.ufrj.br
Instituto de Pesquisas da Marinha – IPqM, Rua Ipiru nº 2, Ilha do Governador, Rio de Janeiro – RJ, CEP 21931–090.
Theodoro Antoun Netto, e-mail: tanetto@lts.coppe.ufrj.br
Programa de Engenharia Oceânica – COPPE/UFRJ, Bloco C do Centro de Tecnologia – Ilha do Fundão, Rio de Janeiro – RJ.

Abstract. *Pipes used in nuclear facilities or for oil transportation can eventually experience serious problems after some years of operation. The evaluation of the defects caused by corrosion in these pipes is important when deciding for the repair of the line or continuity in operation. Under normal operational conditions, these pipes are subject to constant internal pressure and cyclic load due to bending and/or tension. Under such loading conditions, the points in the pipes with thickness reduction due to corrosion are subject to the phenomenon known as ratcheting. The objective of this paper is to present a revision of the available numerical models to treat the ratcheting phenomenon and to develop experimental tests to determine the occurrence of ratcheting in corroded pipes under typical operational load conditions.*

Keywords*: ratcheting, cyclic load, pipes.*

1. INTRODUCTION

Pipes used in the production and export of petroleum may eventually present problems after some years of use due to the presence of corrosion damages under the effect of cyclic loads such as the action of waves and currents or variations of fluid temperature. Evaluation of the defects caused by corrosion is important to help decide for the repair of the line or continuity in operation.

The effect of corrosion damages in the rupture pressure of pipes has been widely studied in recent years. However, under conditions of cyclic loading, the points in the pipes with thickness reduction can suffer the phenomenon known as ratcheting, which is not taken into account in current norms for evaluation of integrity of corroded pipes.

The objective of this paper is to present some numerical models that approach the phenomenon of ratcheting (Armstrong and Frederick, 1966, and Chaboche, 1986, 1991, 1994) and to develop experimental tests in reduced scale reproducing the operational conditions of these pipes, to study the possibility of occurrence of ratcheting (Silveira, 2005).

2. PLASTICITY MODELS FOR RATCHETING

Nowadays we have a growing number of constituent models developed to study the ratcheting response (cyclic accumulation of plastic strains). In many of these models the plastic modulus calculation is coupled with its kinematic hardening rule through the yield surface consistency condition. These models are called coupled models (Bari and Hassan, 2000). The models proposed by Armstrong and Frederick (1966) and Chaboche (1986, 1991, 1994), studied in this paper, belong to this class.

The plasticity models assuming a loading rate independent material behavior have the following common features:

1ª) von Mises yield criterion:

$$f(\boldsymbol{\sigma}-\boldsymbol{\alpha})=\left[\frac{3}{2}(\mathbf{s}-\mathbf{a})\bullet(\mathbf{s}-\mathbf{a})\right]^{1/2}=\sigma_0 \qquad (1);$$

2ª) flow rule:

$$\mathrm{d}\boldsymbol{\varepsilon}^p=\frac{1}{H}\left\langle\frac{\partial f}{\partial\boldsymbol{\sigma}}\bullet\mathrm{d}\boldsymbol{\sigma}\right\rangle\frac{\partial f}{\partial\boldsymbol{\sigma}} \qquad (2);$$

where, $\boldsymbol{\sigma}$ is the stress tensor, $\boldsymbol{\varepsilon}^p$ is the plastic strain tensor, $\mathbf{s}$ is the deviatoric stress tensor, $\boldsymbol{\alpha}$ is the current center of the yield surface, $\mathbf{a}$ is the current center of the yield surface in the deviatoric space, σ_0 is the size of the yield surface (constant for a cyclically stable material), and $\boldsymbol{H}$ is the plastic module.

3ª) the third and most important feature for ratcheting simulation, the kinematic hardening rule is given by:

$$d\mathbf{a} = g(\boldsymbol{\sigma}, \boldsymbol{\varepsilon}^p, \mathbf{a}, d\boldsymbol{\sigma}, d\boldsymbol{\varepsilon}^p, \text{etc}) \quad (3).$$

The kinematic hardening rule dictates the evolution of the yield surface during a plastic loading increment only by translation in the stress space.

In coupled models, the plastic module ***H*** is evaluated using the consistency condition, $\dot{f} = 0$, kinematic hardening rule, Eq. (3), flow rule, Eq. (2), and yield criterion, Eq. (1).

2.1. Non-linear kinematic hardening model

The best known non-linear kinematic hardening model was proposed by Armstrong and Frederick (1966). They introduced a kinematic hardening rule that contains a "recall term", which incorporates the fading memory effect of the strain path and essentially makes the rule nonlinear in nature:

$$d\mathbf{a} = \frac{2}{3} C d\boldsymbol{\varepsilon}^p - \gamma \mathbf{a} dp \quad (5),$$

where

$$dp = \left| d\boldsymbol{\varepsilon}^p \right| = \left[\frac{2}{3} d\boldsymbol{\varepsilon}^p \bullet d\boldsymbol{\varepsilon}^p \right]^{1/2} \quad (6).$$

For uniaxial loading, this rule basically provides an exponential α_x trace [see Fig. 1(a)], which always starts with a modulus given by:

$$H = C \mp \gamma \alpha_x \quad (7)$$

and stabilizes to a value of C/γ after going through some amount of plastic strains. In Equation (7), the negative sign is used for a forward loading curve and the positive sign for a reverse loading curve. Figure 1(a) shows this model simulation of a stable hysteresis loop. It is apparent from the figure that the experimental stress-strain curve is not necessarily exponential in nature and the attempt to simulate it by a single exponential equation is not adequate. Increasing the value of *C* the simulation during the initial non-linear phase would be improved, but the simulation for the rest of the curve would suffer. Another limitation of this model is its inability to produce constant plastic modulus exhibited on experiments with a high strain range. This model stabilizes with plastic modulus equal to zero.

For an uniaxial stress cycle with average stress, the “recall” term in the Armstrong and Frederick kinematic hardening rule produces changes in shape between forward and reverse loading paths. Therefore, the loop does not close and results in ratcheting [see Fig. 1(b)]. But the stress – strain loop produced by this model deviates significantly from the experiment and the ratcheting strain is also over predicted, as demonstrated in Fig. 1(b).

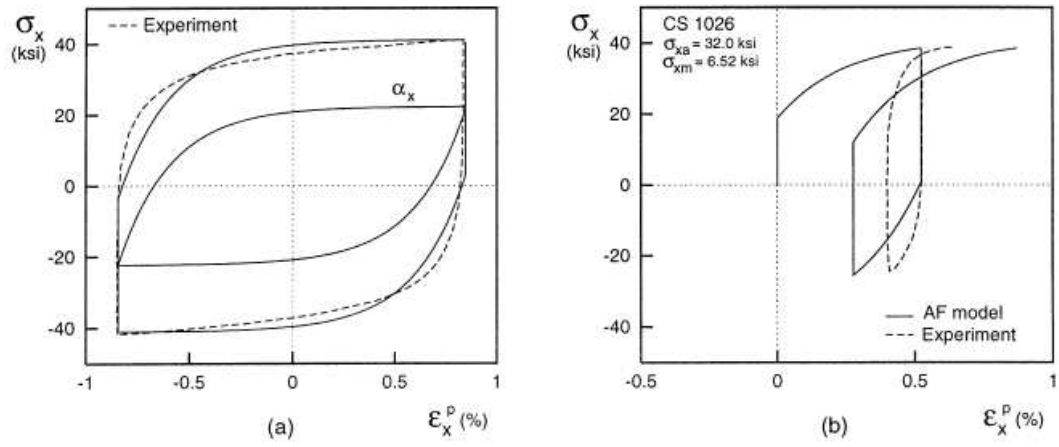

Figure 1. Predictions from Armstrong and Frederick model (AF) for (a) strain-controlled stable hysteresis loop, (b) stress-controlled hysteresis loop (Bari and Hassan, 2000).

2.2. Chaboche model with three decomposed rules

Chaboche in Chaboche *et al.* (1979) and Chaboche (1986) proposed a non-linear kinematic hardening rule "decomposed" in the form:

$$\mathrm{d}\mathbf{a} = \sum_{i=1}^{M} \mathrm{d}\mathbf{a}_i \;\therefore\; \mathrm{d}\mathbf{a}_i = \frac{2}{3} C_i \mathrm{d}\boldsymbol{\varepsilon}^p - \gamma_i \mathbf{a}_i \mathrm{d}p \tag{8}$$

and

$$\mathrm{d}p = \left|\mathrm{d}\boldsymbol{\varepsilon}^p\right| = \left[\frac{2}{3}\mathrm{d}\boldsymbol{\varepsilon}^p \bullet \mathrm{d}\boldsymbol{\varepsilon}^p\right]^{1/2} \tag{9}.$$

As can be observed in Eq. (8), the Chaboche kinematic hardening rule is a superposition of several Armstrong and Frederick hardening rules. Each of these decomposed rules has its specific purpose.

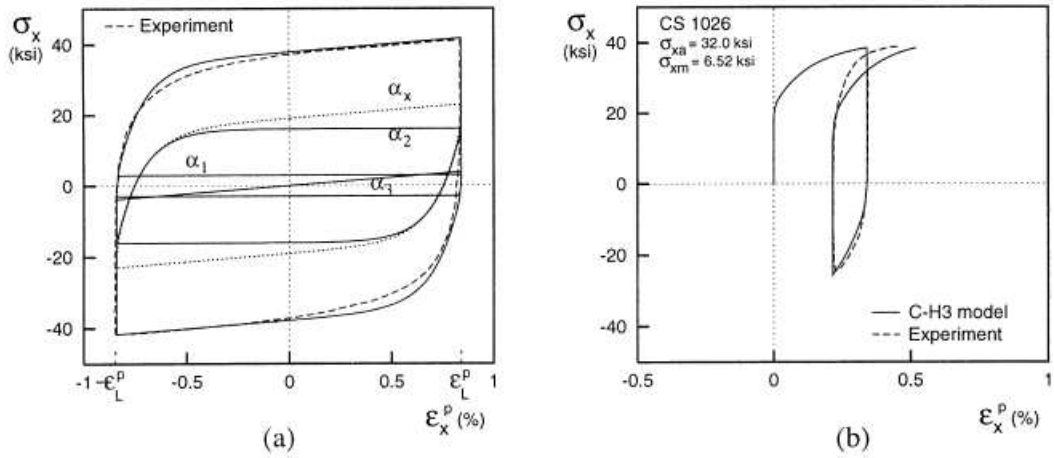

Figure 2. Predictions from Chaboche model with 3 decomposed rules (C-H3) for (a) strain-controlled stable hysteresis loop, (b) stress-controlled hysteresis loop (Bari and Hassan, 2000).

A stable hysteresis curve can be divided into three critical segments where the Armstrong and Frederick model fails: the initial high modulus at the onset of yielding, the constant modulus segment at a higher strain range and the short non-linear segment [knee of the hysteresis curve, see Fig. 1(a)]. Chaboche (1986) proposed to use initially three decomposed hardening rules [M = 3 in Eq. (8)] to improve the simulation of the hysteresis loops in these three segments. He suggested that the first rule (α_1) should start hardening with a very large modulus and stabilize very quickly. The second rule (α_2) should simulate the short non-linear portion of the stable hysteresis curve. Finally, the third rule (α_3) should be a linear hardening rule $(\gamma_3 = 0)$ to represent the subsequent linear part of the hysteresis curve at a high strain range. If this scheme is followed, the simulation for a stable hysteresis loop improves as shown in Fig. 2(a) [compared to Fig. 1(a)]. Figure 2(a) presents the traces of the three decomposed rules (α_1); (α_2) and (α_3) and the resulting yield surface center $\alpha_x (= \alpha_1 + \alpha_2 + \alpha_3)$. The hysteresis curve simulation still deviates slightly from the experimental curve. This can be improved further by adding more kinematic rules as it is discussed later.

Figure 2(b) shows the simulation for a stress-controlled hysteresis loop by the Chaboche model using three decomposed rules. This simulated hysteresis loop shows a significant improvement from that presented by the original Armstrong and Frederick model and it is very close to the experimental loop. But this model still over predicts the ratcheting strain at the end of the first cycle.

2.3. Chaboche model - fourth rule with a threshold

Realizing the previous deficiencies of the model, CHABOCHE [3] added to it a fourth hardening rule with a concept of "threshold". This kinematic hardening rule grows linearly to a certain "threshold" stress level and subsequently hardens according to the Armstrong and Frederick rule, as follows:

$$d\mathbf{a}_i = \frac{2}{3} C_i d\varepsilon^p - \gamma_i \mathbf{a}_i \left\langle 1 - \frac{\bar{a}_i}{f(\alpha_i)} \right\rangle dp \qquad \text{for } i = 4 \tag{10}.$$

This fourth rule simulates a constant linear hardening with a slope of C_4 within the threshold $\pm \bar{a}_4$ and becomes non-linear outside the threshold [see α_4 trace in Fig. 3(a)].

When this fourth rule is added to the previous three decomposed rules, the model predicts a reduced rate of ratcheting for initial cycles without committing the simulation of the stable hysteresis loop. The improvement becomes evident if simulations in Fig. 2, letters (a) and (b) are compared to Fig. 3, letters (a) and (b), respectively. The simulation in Fig. 3(b) conforms better with the experimental uniaxial ratcheting hysteresis loop when compared to that in Fig. 2(b).

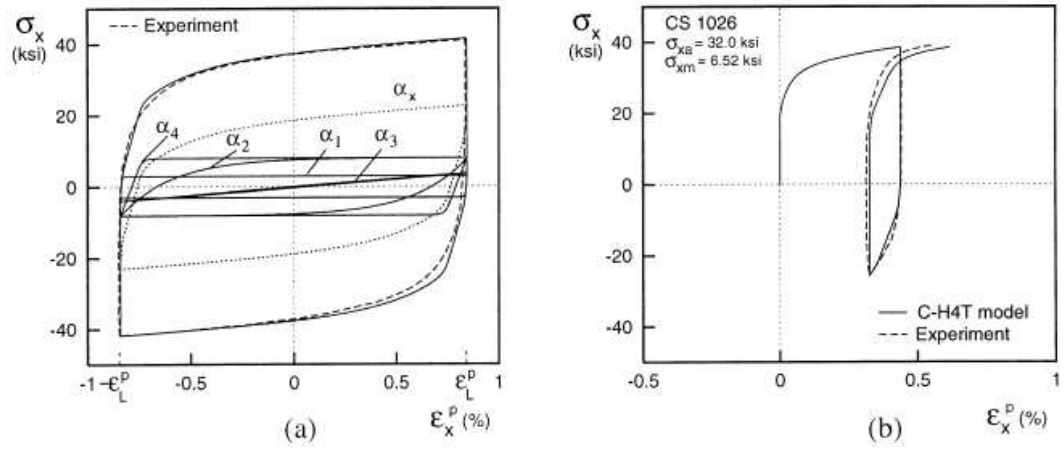

Figure 3. Predictions from Chaboche model with "threshold" (C-H4T) for (a) strain-controlled stable hysteresis loop, (b) stress-controlled hysteresis loop (Bari and Hassan, 2000).

The reason for the improvement in uniaxial ratcheting simulation, when the fourth rule with a "threshold" is used, is because within the threshold level, this rule does not use its recall term and assumes linear hardening. The linear hardening acts as instrument in stiffening the loading curves and relaxing the unloading curves to reduce completely ratcheting with cycles. When the threshold level is reached, the hardening becomes non-linear again and the reduction of ratcheting is attenuated to avoid potential shakedown. The threshold level, $\bar{a}_4$ can also be considered a ratcheting parameter which will be determined from uniaxial ratcheting experiments.

3. EXPERIMENTS

The experiments were developed with two purposes: to reproduce in reduced scale the operational conditions of the pipes used in petroleum exploration to determine the occurrence of ratcheting and to make a comparison with the numeric model used.

3.1. Material properties

The material properties were established through monotonic uniaxial tensile tests, showed in Fig 4, applied to specimens removed in the longitudinal direction of the pipe used to make the models.

The material yield and rupture strength, as well as the elasticity modulus and the Poisson's coefficient are presented in the Tab. 1.

Table 1. Material Properties.

Yield Limit at 0,2%:	$\sigma_0 =$	279 MPa
Rupture strength:	$\sigma_r =$	490 MPa
Elasticity modulus:	$E =$	195 GPa
Poisson's Coefficient:	$\nu =$	0,3

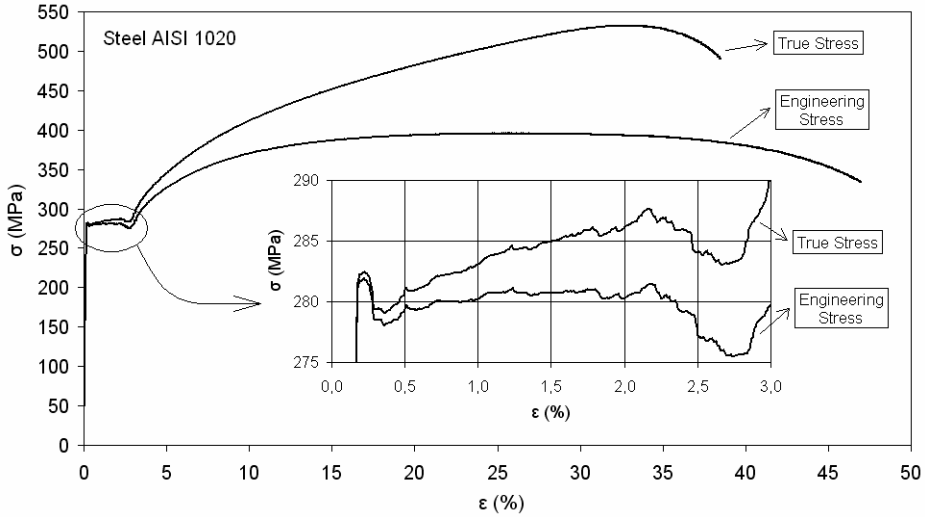

Figure 4. Stress-strain curve obtained from monotonic uniaxial tensile tests.

3.2. Cyclic tests models

For the cyclic bending tests at constant internal pressure specimens were manufactured with three different defect sizes, as shown in Tab. 2 and Fig. 5.

Table 2. Dimensions of the defects manufactured in the specimens tested

	Model 1	Model 2	Model 3
Nominal external diameter of the pipe (D)	42,0 mm	42,0 mm	42,0 mm
Nominal thickness of the wall of the pipe (t)	2,7 mm	2,7 mm	2,7 mm
Length of the defect (LD)	1 x D	1 x D	1 x D
Depth of the defect (h)	0,6 x t	0,7 x t	0,8 x t

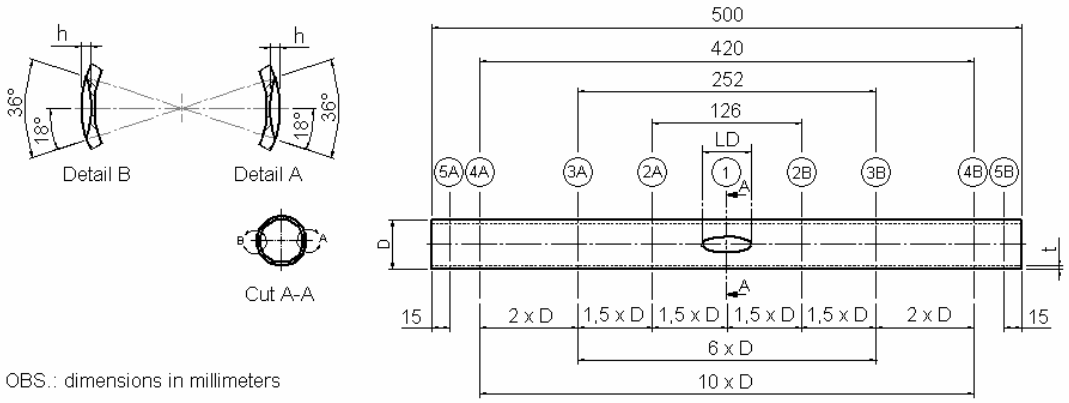

Figure 5. Specimen for cyclic test.

As can be seen in Fig. 5 each model presents two longitudinal defects, equal and diametrically opposed, simulating corrosion defects. Two specimens of each model were manufactured, totaling, therefore, six specimens. Each model was divided along its length in nine sections (1, 2A, 2B, 3A, 3B, 4A, 4B, 5A, 5B), and each section divided in 18° segments along the perimeter. Before machining the defects, the dimensions (diameter with micrometer and thickness with ultrasound) of the points marked in sections 1, 2A, 2B, 3A, 3B, were measured. The points of sections 5A and 5B were used for ultrasound calibration. This calibration was made comparing the value of the pipe wall thickness obtained by ultrasound with the value measured with a micrometer of spherical tips in each point of the section.

The defects were machined by electro-erosion (to avoid stress concentration) in section 1 positioned in the center of the model, in the diametrically opposite points that presented the smallest thickness difference. After electro-erosion, the depth of the defects was measured with the aid of a clock gauge.

3.3. Cyclic Test

The equipments and materials used in the cyclic tests are presented in Fig. 6 and listed below.

(1) INSTRON Fatigue Testing Machine, model 8802;
(2) Device for application of the cyclic bending load (four-point bending);
(3) Device for application of the internal pressure (set up inside of the specimen);
(4) Device for operator protection in the case of rupture of the pressurized specimen;
(5) INSTRON Load Cell (capacity up to 25 kN);
(6) Pressure Transducer (capacity up to 5000 psi);
(7) LVDT Displacement Transducer (capacity up to 10 mm);
(8) Specimen;

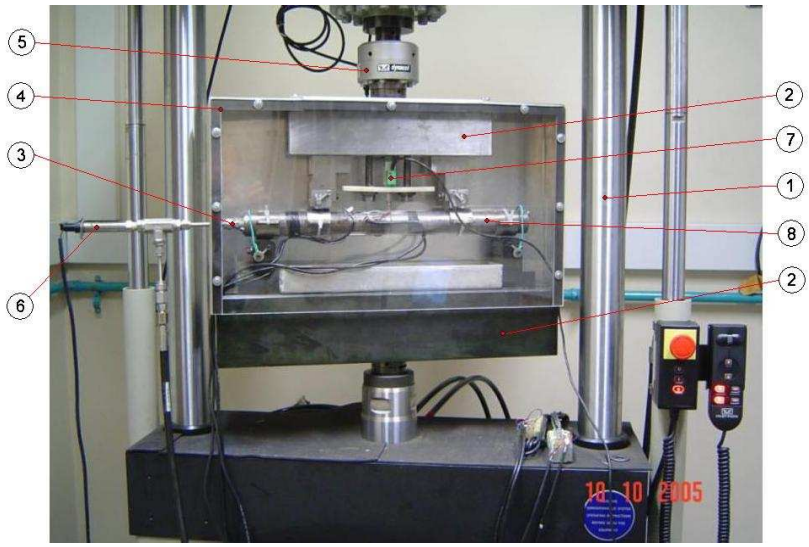

Figure 6. Cyclic bending test at constant internal pressure.

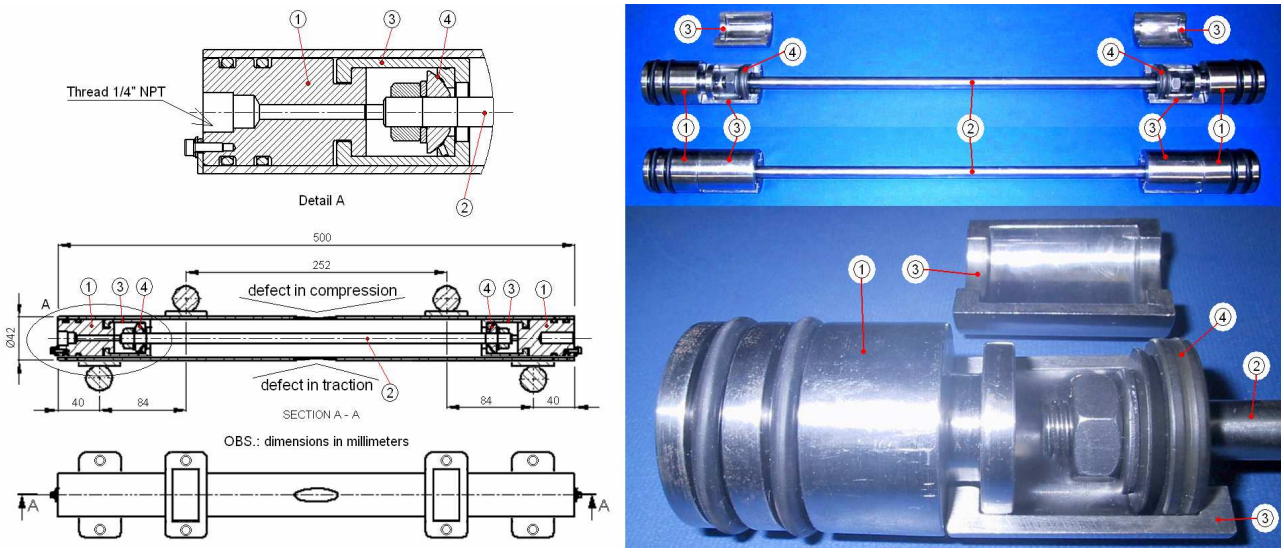

Figure 7. Device for application of internal pressure.

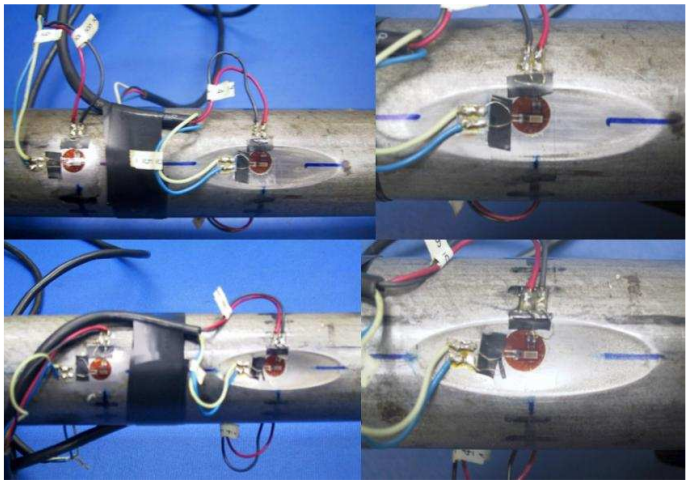

Figure 8. Biaxial Strain Gages.

The device for internal pressure application was developed in such a way as to allow that the pressure applied to accomplish the test cause only circumferential stress to the specimen without increasing its rigidity at longitudinal bending. As can be seen in Fig. 7 the extremities of the device (1) are not fixed to the specimen but are united through an axis (2) with two bipartite coupling (3) and two kneecaps (4).

In each specimen four biaxial strain gages (each strain gage has 2 mm of length for 1 mm of width) were placed as shown in Fig. 8, one in each defect and two in section 2A or 2B (see Fig. 5), aligned with the defects (same angle of circumferential positioning), in order to measure the circumferential and longitudinal strain in the center of the defects and in an area submitted to the same loading, but without defect (section 2A or 2B). Strain gages were placed out of the area of the defect, to allow a comparison with the obtained results of the numerical analysis (with data of the elements that are positioned at the same place of the strain gages), and with the result of the analysis of a bi-supported beam (presented in Fig. 9) with internal pressure. The results are presented in Tab. 3.

Table 3. Deformation in the area without defect for medium load test (9,02 kN).

		TEST	ABAQUS	BEAM
Circumferential Strain ε_θ (%)	Compression Stress	0,073	0,073	0,072
	Tensile Stress	0,030	0,033	0,034
Longitudinal Strain ε_z (%)	Compression Stress	- 0,077	- 0,077	- 0,079
	Tensile Stress	0,051	0,049	0,047

In the analysis of the bi-supported beam the following equations were used:

$$\varepsilon_\theta = \frac{1-\nu}{E}\sigma_\theta - \frac{\nu}{E}(\sigma_z + \sigma_\theta) \quad (20),$$

$$\varepsilon_z = \frac{1-\nu}{E}\sigma_z - \frac{\nu}{E}(\sigma_z + \sigma_\theta) \quad (21),$$

$$\sigma_\theta = \frac{p\mathrm{d}}{2\mathrm{t}} \quad (22),$$

$$\sigma_z = \frac{M\mathrm{D}}{2\mathrm{I}} \quad (23),$$

$$M = Fa \quad \text{[see Fig. 9]} \quad (24)$$

and

$$\mathrm{I} = \frac{\pi}{64}\left(\mathrm{D}^4 - \mathrm{d}^4\right) \quad (25)$$

where ν and *E* are the material Poisson Coefficient and Elasticity Modulus, respectively, presented in Tab. 1. Other parameters are: the pipe wall nominal thickness, t, the external diameter of the pipe, D, the internal diameter of the pipe, d, the internal pressure, *p*, the bending moment, *M*, and the moment of inertia, I, of the pipe.

After the strain gage gluing and instrumentation, the device of internal sealing is assembled inside the specimen which is then positioned in the apparatus of application of the bending load so that the defects are aligned vertically. In this way, the defect positioned above the horizontal plan that passes by the axis of the specimen will be submitted to compression stress and the defect positioned below the horizontal plan that passes by the axis of the specimen will be submitted to tensile stress (during the cyclic bending loading, see Fig. 7). It should be emphasized that because of the internal pressure and the cyclic bending loading, the defect submitted to the compression stress is subject of a negative longitudinal stress (σ_z), resulting in a circumferential strain (ε_θ) larger than for the defect submitted to the tensile stress. This observation can be verified in the elastic regime, for instance, analyzing the second term on the right side of Eq. (20).

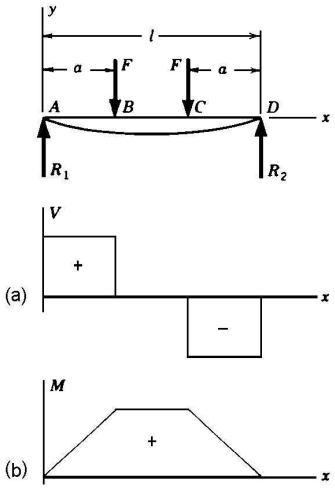

Figure 9. Bi-supported beam with two same loads and equally spaced: (a) “Cutting Effort” diagram and (b) Bending moment diagram.

During the essays the specimens were submitted to an equivalent stress, σ_{eq}, between 30% and 90% of the material yield limit, σ_0 (presented in Tab. 1), represented by the following equation:

$$\sigma_{eq} = \sqrt{3J_2} \therefore J_2 = \frac{1}{6}\left[(\sigma_z - \sigma_\theta)^2 + \sigma_\theta^2 + \sigma_z^2\right] \quad (26).$$

The result of the cyclic test is presented in Fig. 10, circumferential strain vs. number of cycles, for a load of 9,02 kN.

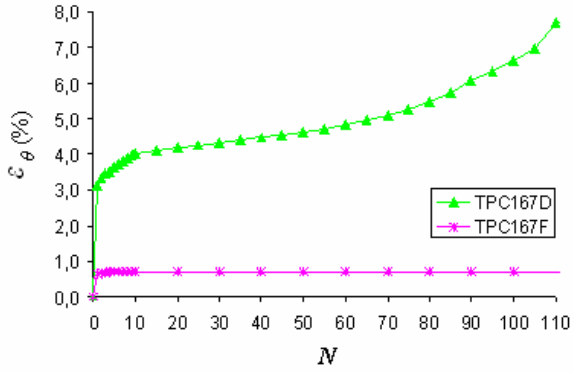

Figure 10. Circumferential Strain x Number of cycles: defect in compression stress.

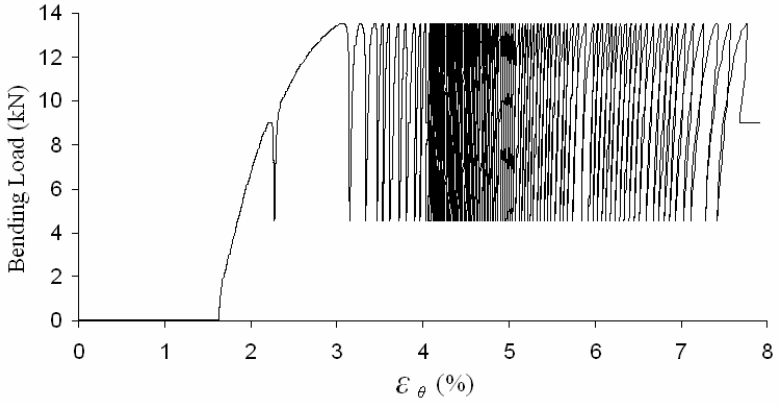

Figure 11. Load x Strain curve of the specimen TPC167D with 110 cycles.

Figure 11 presents the Load x Strain curve obtained with the specimen TPC167D that possesses the largest defect depth, where the occurrence of ratcheting can be observed and Fig. 12 presents the Load x Strain curve obtained with the specimen TPC167F that possesses the smallest defect depth, where the occurrence of shakedown can be observed.

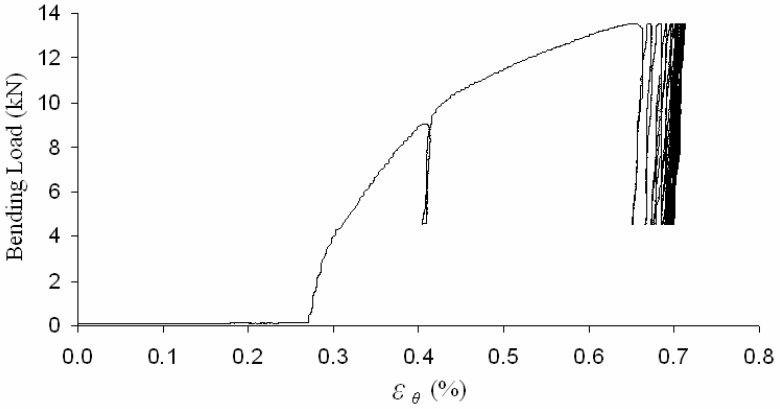

Figure 12. Load x Strain curve of the specimen TPC167F with 110 cycles.

4. NUMERICAL ANALYSIS

As presented in item 3 cyclic bending tests were done in four points, at constant internal pressure in pipe samples with elliptic defects produced by electro-erosion. To simulate those tests, three numerical models (one for each defect depth, according to Tab. 2) were made, based on the finite elements method through the commercial software ABAQUS version 6.3.5 installed in Workstation Sun Blade 1000 of the Laboratory of Underwater Technology (LTS) – COPPE / UFRJ.

Analyzing the diagrams of "Cutting Effort" and "Bending Moment" of a bi-supported beam model with two equal loads and equally spaced (the configuration of the realized tests) presented in Fig. 9, we can conclude that between points B and C there is a null cutting effort and constant bending moment. This fact allowed creating a simpler numerical model. Fig 9 points B and C correspond to Fig 5 points (3A) and (3B). The distance between the points (3A) and (3B) is six times the specimen diameter and as the sample possesses longitudinal and transversal symmetry, the numerical models could be reduced to 1/4 the sample dimension between the points (3A) and (3B) of Fig. 5.

As can be seen in Fig. 13, the model presents symmetry in relation to the transversal plan that passes by the center of the model (and of the defect), parallel to the plan 1-2 of the system of global coordinates and to the vertical plan coincident with the plan 2-3 of the global coordinates system.

In the numerical analysis, the loading was applied in two steps: in the first step pressure was applied in the internal face of the model, as can be seen in Fig. 14(a) and in the second step, the pressure applied in the previous step was maintained constant and a cyclic moment was applied in a knot positioned in the reference point (RP). This knot is connected to all the existent knots in the transversal face of the model equivalent to section (3B) of Fig. 5, as can be seen in Fig. 14(b).

The mesh of finite elements was generated starting from the three-dimensional solid element C3D20 (quadratic element) that possesses twenty knots and twenty-seven integration points.

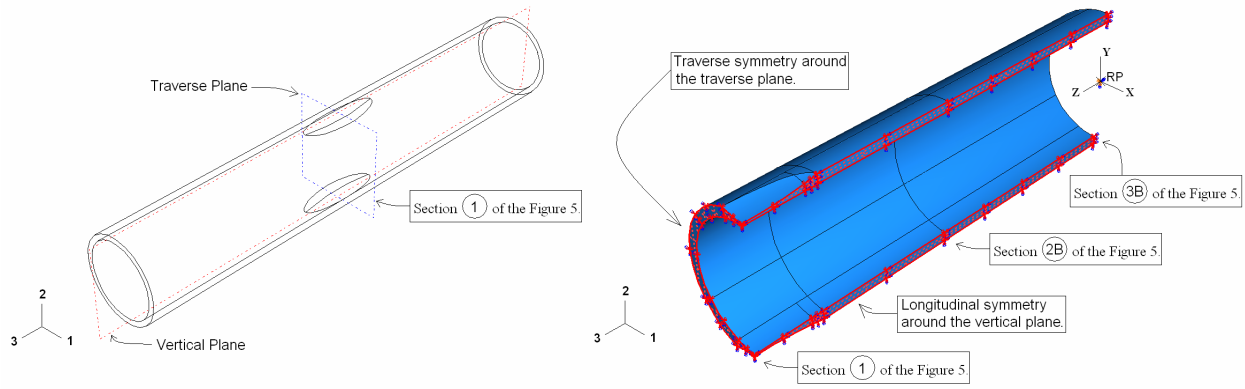

Figure 13. Symmetry of the numerical model.

The active degrees of freedom were the three translation components in each knot (Ux, Uy, Uz) and the three rotation components in each knot (URx, URy, URz).

In the resolution, full integration and the ABAQUS non-linear isotropic / kinematic hardening model based on the work of Lemetre and Chaboche (1990) were used.

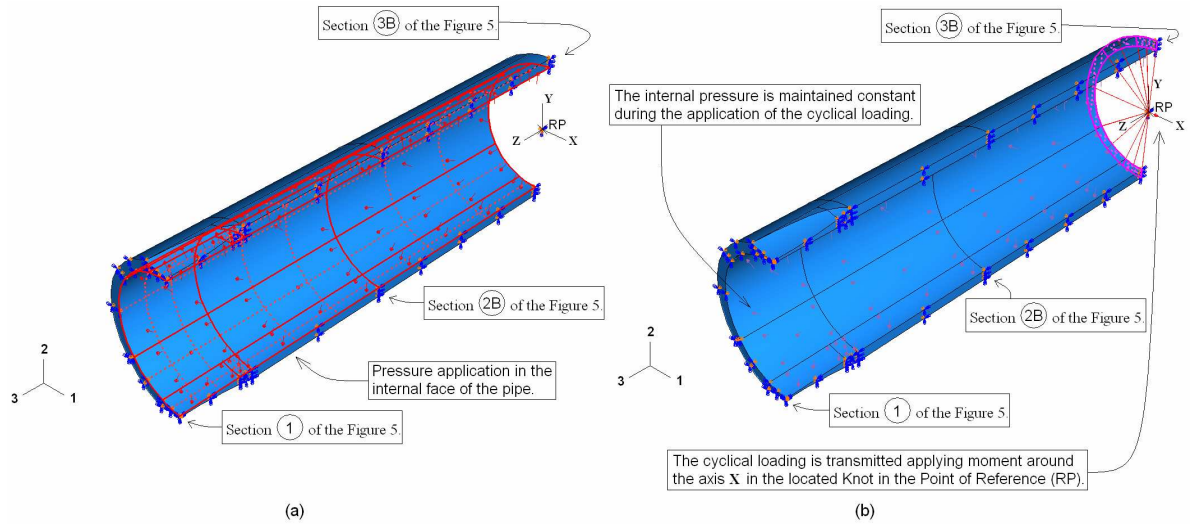

Figure 14. Applied loading: (a) 1st load step and (b) 2nd load step.

This model was calibrated with the results of the experimental monotonic uniaxial tensile tests presented in Tab. 1. In these conditions, the model is recommended for simulations that involve few loading cycles, what met the computational capacity available (processing speed and storage capacity). For this reason, only ten bending cycles were applied. The model used by ABAQUS presents better results if gauged by the cyclic stress – strain curve of the material; however the obtainment of this curves is quite complex and slow, and that kind of calibration was not used in this paper.

The only mesh difference between the three numerical models is the depth of the defect. The thickness of the pipe wall used in the three numerical models was 2.7 mm. Along the thickness the mesh was divided in four elements. The total length of the numerical model was of 126 mm (3D) [space between the points (1) and (3B) of Fig. 5]. Along the length the mesh was divided in three sections, being the first equal to the length of half of the defect (21 mm), it was divided in twelve 1.75 mm elements. The second section, with length equal to the size of the defect (42 mm), was divided in twelve 3.5 mm elements and the last section, being equal to the points (2B) and (3B), of Fig. 5 (63 mm = 1.5D), was divided in nine 7 mm elements. Circumferentially the mesh was divided in five sections, being two with 18° corresponding to half of each defect; they were divided in eight elements of 2.25°. The two sections adjacent to the defects with 36° were divided in eight 4.5° elements, and the fifth section, with 72°, was divided in eight elements of 9°. A typical mesh is shown in Fig. 15.

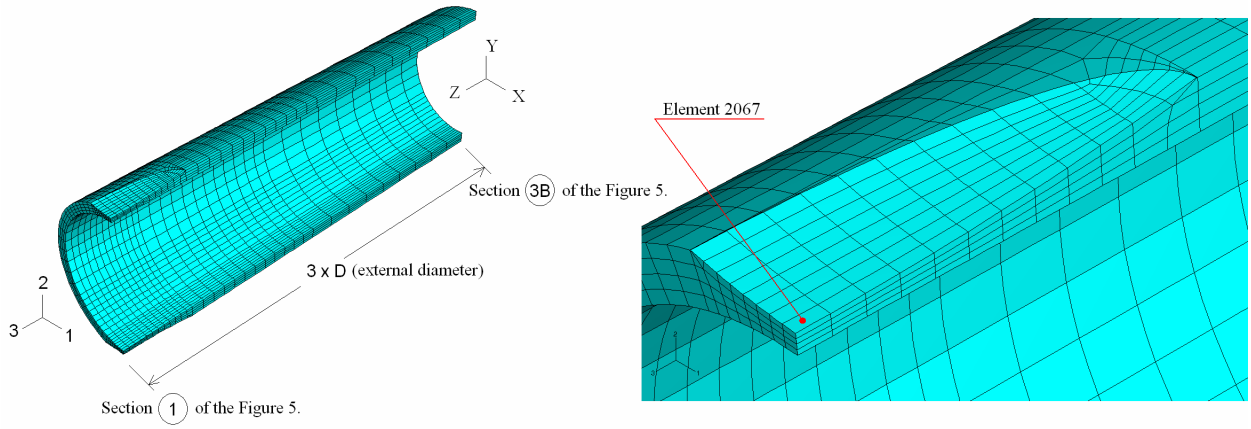

Figure 15. Finite element mesh of Model 1.

5. NUMERICAL / EXPERIMENTAL CORRELATION

The numerical results were obtained from an average of the integration points of the element at the center of each defect. Figure 16 presents the numbering of the knots of the element 2067 and Tab. 4 presents the values of circumferential strain obtained in the integration points close to the knots that correspond to the position of the transversal strain gage used in the tests.

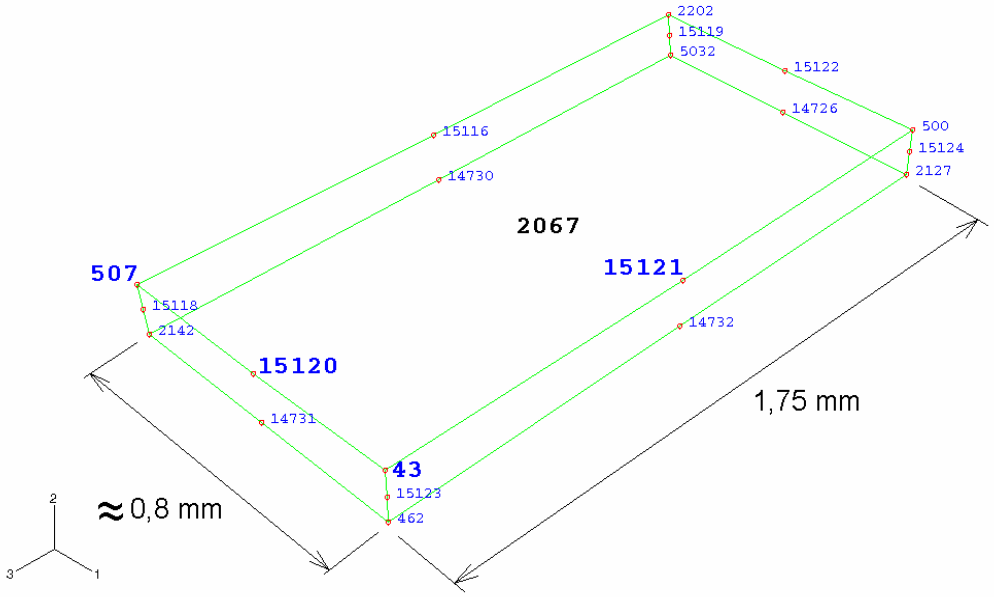

Figure 16. Numbering of the knots of the element 2067 of Model 3.

Table 4. Circumferential and Longitudinal Strains for the medium load of bending: 9,02 kN.

MODEL 3 – ELEMENT 2067			
KNOT OF THE ELEMENT 2067	POINT OF INTEGRATION CLOSE TO THE KNOT	CIRCUNFERENTIAL STRAIN $\varepsilon_{\theta 1}$ (%)	LONGITUDINAL STRAIN ε_{z1} (%)
507	19	2,646	----------
15120	20	3,871	----------
15121	24	----------	- 0,248
43	21	5,105	- 0,250
	MEDIUM	3,874	- 0,249

The values presented in Tab. 4 show the great gradient of deformation that exists in the center of the defect for the case of circumferential strain. In the defect, the pipe wall thickness varies in a more accentuated way in the circumferential direction than in the longitudinal direction. Therefore, in the circumferential direction a great variation of the deformation values exists among the integration points, that does not happen in the longitudinal direction.

Table 5 presents the deformations after the first loading cycle (load of 9,02 kN) of the defect in compression of the specimens TPC167D and F (numeric and experimental results).

Table 5. Numeric / experimental correlation: values of the deformations in the defect in compression stress after the 1st loading cycle (load of 9,02 kN).

Specimen	Model (Table 2)	Circumferential Strain $\varepsilon_{\theta 1}$ (%)	Longitudinal strain ε_{z1} (%)
ABAQUS	1	0,845	- 0,155
	3	3,874	- 0,249
TPC167D	3	3,138	- 0,350
TPC167F	1	0,658	- 0,256

The differences between the values of the deformations obtained by the numerical model and measures in the specimens can be attributed to the range of values where these deformations occurred. Observing the curve of the material presented in item 3.1, Fig. 4, the existence of a platform can be verified, where a great strain variation (0.2% to 3.0%) occurs for a small stress variation (275 to 290 MPa).

The circumferential strains measured in the specimens are between 0.2% and 3.0%, therefore inside of this range. The only exception was observed for the deepest defect, submitted to the compression stress (specimen TCP167D), where ratcheting occurred with a maximum deformation measured of approximately 7.75% (see Fig. 10), not captured by the numerical model (see Fig. 17).

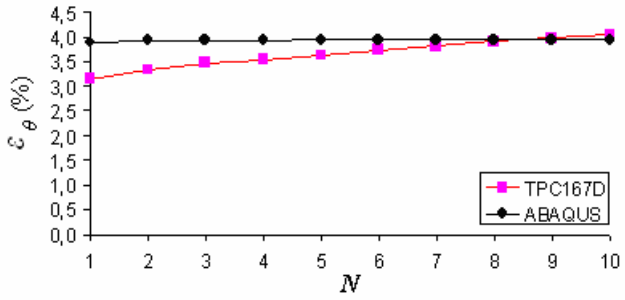

Figure 17. Circumferential Strain x Number of cycles of the Model 3: defect in compression stress (load of 9,02 kN).

6. CONCLUSIONS

The present paper concentrates in the study of the effect of the loss of pipe thickness due to the corrosion process and on its resistance in relation to the cyclic loads of operation of the line originated from thermal variations, seismic loads or waves and marine currents.

The analysis of the experimental results showed that only in the deepest defect (80% of the thickness of the wall of the pipe) and with a loading varying between 30% and 90% of the yield limit of the material ratcheting was observed. It was not possible to verify its stabilization soon due to the rupture of the strain gage in the beginning of the test (with 110 cycles). For the other specimens, the shakedown happened almost immediately.

Therefore, the possibility of occurrence of ratcheting in corroded pipes under cyclic loading should be considered when of the analysis of the structural integrity during its useful life, depending on the loading and on the size of the defect.

In parallel to the experimental tests, a three-dimensional finite element model was developed with the commercial software ABAQUS (version 6.3.5) with the purpose of simulating the occurrence or not of the phenomenon known as ratcheting. The constitutive model used by ABAQUS obtained good correlation for the deformations presented in the first cycle of the cyclic bending loading (equal to a monotonic uniaxial tensile tests), it foresaw the shakedown presented in the specimens with depth of defect of 60% and 70% of the thickness of the wall of the pipe, but it did not get to foresee the ratcheting that occurred in the deepest defect. The fact that the numerical model was gauged starting from monotonic uniaxial tensile tests to counterpoint the triaxiality of the state of tensions in the models in the defect area can partially explain these results.

4. REFERENCES

Armstrong, P. J., Frederick, C. O., 1966, "A mathematical representation of the multiaxial bauscinger effect". CEGB Report No. RD/B/N 731.

Bari, S., Hassan, T., 2000, "Anatomy of coupled constitutive models for ratcheting simulation", International Journal of Plasticity, v. 16, pp. 381 – 409.

Chaboche, J. L., 1986, "Time-independent constitutive theories for cyclic plasticity", International Journal of Plasticity, v. 2, pp. 149 – 188.

Chaboche, J. L., 1991, "On some modifications of kinematic hardening to improve the description of ratcheting effects", International Journal of Plasticity, v. 7, pp. 661 – 678.

Chaboche, J. L., 1994, "Modeling of ratchetting: evaluation of various approaches", European Journal of Mechanics, A / Solids, v. 13, pp. 501 – 518.

Chaboche, J. L., Dang-Van, K., Cordier, G., 1979, "Modelization of the strain memory effect on the cyclic hardening of 316 stainless steel". In: Proceedings of the 5th International Conference on SMiRT, Div. L, Berlin, Germany.

Lemetre, J, Chaboche, J. L., 1990, Mechanics of solid materials. 1 ed. English translation, Cambridge, Great Britain, Cambridge University Press.

Silveira, M. A. B. N., 2005, "Colapso Incremental de Dutos Corroídos Pressurizados Internamente Sob Flexão Alternada: Revisão de Métodos Numéricos e Desenvolvimento de Testes Experimentais". Tese de M.Sc., COPPE / UFRJ, Rio de Janeiro, RJ, Brasil.

5. RESPONSIBILITY NOTICE

The authors are the only responsible for the printed material included in this paper.